

Cite this: *Mater. Horiz.*, 2021,  
8, 3432Received 23rd August 2021,  
Accepted 11th October 2021

DOI: 10.1039/d1mh01370j

rsc.li/materials-horizons

# Room-temperature synthesis of blue-emissive zero-dimensional cesium indium halide quantum dots for temperature-stable down-conversion white light-emitting diodes with a half-lifetime of 186 h†

Fei Zhang, Xinzhen Ji, Wenqing Liang, Ying Li, Zhuangzhuang Ma, Meng Wang, Yue Wang, Di Wu, Xu Chen, \* Dongwen Yang, Xinjian Li, Chongxin Shan and Zhifeng Shi \*

Recently, the newly-emerging lead halide perovskite quantum dots (QDs) have attracted intensive research interest for lighting and display applications owing to their remarkable optoelectronic properties. It is regrettable that the toxicity and instability of lead largely hinder their practical applications. Here, zero-dimensional (0D) cesium indium halide ( $\text{Cs}_3\text{InX}_6$ ) QDs were synthesized for the first time using a modified ligand-assisted reprecipitation method, and the emission wavelength can be tuned facilely via an anion exchange reaction. Typically, the  $\text{Cs}_3\text{InBr}_6$  QDs showed broadband blue emission with a high photoluminescence (PL) quantum yield of 46%. First-principles calculations were performed and temperature-dependent PL was studied to investigate the emission mechanisms of the  $\text{Cs}_3\text{InBr}_6$  QDs; the 0D nature of  $\text{Cs}_3\text{InBr}_6$  enhances the localization of excitons, resulting in a large exciton binding energy. It is worth noting that the strong electron-phonon coupling of  $\text{Cs}_3\text{InBr}_6$  indicates that the broadband emission comes from self-trapped exciton emission. Moreover, the  $\text{Cs}_3\text{InX}_6$  QDs exhibit excellent stability against moisture, ultraviolet light and heat degradation, significantly better than for conventional lead halide perovskites. Subsequently, the white light-emitting diodes (WLEDs) prepared using blue-emissive  $\text{Cs}_3\text{InBr}_6$  QD powder used as the phosphor showed an excellent working stability with a record half-life ( $T_{50}$ ) of 186 h. Even if the operating temperature is as high as 106.9 °C, the LED can still operate well and reach a  $T_{50}$  of 50 h. These results highlight the huge advantages and application potential of 0D  $\text{Cs}_3\text{InX}_6$  QDs as an environmentally friendly emitter in the field of solid-state lighting.

## New concepts

Lead halide perovskite materials with nanoscale geometries have been rapidly developed in light-emitting diodes (LEDs) due to their excellent photoelectric properties, while the blue-emissive materials and devices have struggled to match the high-efficiencies of their green and red counterparts. Even more unfortunately, the inherent toxicity and chemical instability of lead have cast a shadow over their commercial applications. Therefore, it is particularly important to develop lead-free and stable blue-emissive perovskite materials. Here, for the first time, zero-dimensional  $\text{Cs}_3\text{InBr}_6$  quantum dots (QDs) were synthesized using a modified ligand-assisted reprecipitation method, and show broadband blue emission and a high photoluminescence quantum yield of 46%. The emission wavelength was readily tunable over the spectral range of 397–535 nm through an anion exchange strategy. Experimental and theoretical calculation results confirm that the broadband emission characteristics of the  $\text{Cs}_3\text{InBr}_6$  QDs originate from the emission of self-trapped excitons. More importantly, the  $\text{Cs}_3\text{InBr}_6$  QDs show excellent stability, and the white LED produced by the combination of  $\text{Cs}_3\text{InBr}_6$  QD powder and yellow-emissive  $(\text{Ba,Sr})_2\text{SiO}_4:\text{Eu}^{2+}$  also shows a good long-term working stability, producing a long half-lifetime ( $T_{50}$ ) of 186 h at 29.1 °C; moreover, this LED can still function properly at 106.9 °C with a  $T_{50}$  of 50 h. These results indicate that such lead-free and stable QDs can serve as a promising emitter for lighting and display applications.

## Introduction

Since more than 20% of the world's electrical energy is consumed each year through lighting and displays, saving electrical energy and improving energy efficiency are crucial in the field of illumination and are certainly worthwhile subjects.<sup>1</sup> Under these circumstances, solid-state white light-emitting diodes (WLEDs) have received increasingly widespread attention owing to their compact size, low power consumption, and high efficiency compared with traditional lighting equipment, and they are expected to change the lighting methods of houses and businesses.<sup>2–4</sup> In recent years, lead halide perovskite quantum dots (QDs) have attracted much attention as luminescent elements in phosphor-converted

Key Laboratory of Materials Physics of Ministry of Education, School of Physics and Microelectronics, Zhengzhou University, Zhengzhou 450052, China.

E-mail: shizf@zzu.edu.cn, xchen@zzu.edu.cn

† Electronic supplementary information (ESI) available. See DOI: 10.1039/d1mh01370j

WLEDs because of their low-cost synthesis process, wide color gamut, high photoluminescence quantum yield (PLQY) values, continuously tunable fluorescence emission, and narrower full-width at half-maximum (FWHM) values.<sup>5–9</sup> However, most of the previously reported perovskite QDs WLEDs contain the toxic element lead, which has become an obstacle to large-scale production and practical applications in the future.<sup>10–12</sup> Therefore, researchers need to devote themselves to finding lead-free perovskite materials with excellent photoelectric properties, environmental friendliness and stability to solve the above obstacles.

In recent years, using metal cations to replace lead, researchers have developed a series of lead-free perovskite QDs or nanocrystals. Replacing lead with the element tin, which has the same valence state and a similar atomic radius to lead, was initially proposed and maintains the three-dimensional perovskite structure well. It is a pity, however, that CsSnX<sub>3</sub> perovskites are extremely sensitive to the surrounding environment, with tin being easily oxidized to its tetravalent state (Sn<sup>4+</sup>) in air, resulting in a low PLQY.<sup>13,14</sup> Heterovalent substitution of Pb<sup>2+</sup> with other metal cations is another feasible solution to achieve lead-free perovskites. For instance, double perovskite materials form three-dimensional structures by replacing the divalent lead ions with monovalent and trivalent metal cations, including Ag<sup>+</sup>/Bi<sup>3+</sup>, Ag<sup>+</sup>/Sb<sup>3+</sup>, Ag<sup>+</sup>/In<sup>3+</sup>, etc.,<sup>15–19</sup> and much interesting progress in this area has been witnessed in the past three years. In addition, low-toxicity trivalent bismuth and antimony have also attracted considerable attention because of their similar *ns*<sup>2</sup> electronic configurations and atomic radii to Pb. Experimentally, Cs<sub>3</sub>Bi<sub>2</sub>X<sub>9</sub> and Cs<sub>3</sub>Sb<sub>2</sub>X<sub>9</sub> QDs have been synthesized by some groups, and exhibit many attractive features such as a high defect tolerance and good stability.<sup>20,21</sup> Trivalent indium, a group IIIA metal with no toxicity, is another promising candidate for substituting Pb to form lead-free perovskites. Owing to the small ionic radius of In, In-based metal halides tend to form low-dimensional structures. Some previous studies have reported the synthesis of In-based halide bulk single crystals, including A<sub>2</sub>InCl<sub>5</sub>·H<sub>2</sub>O (Rb, Cs), (C<sub>4</sub>H<sub>14</sub>N<sub>2</sub>)<sub>2</sub>In<sub>2</sub>Br<sub>10</sub>, and (C<sub>6</sub>H<sub>5</sub>CH<sub>2</sub>NH<sub>3</sub>)<sub>3</sub>InBr<sub>6</sub>.<sup>22–26</sup> However, at present, such novel lead-free perovskite systems are still rarely studied in the form of colloidal nanomaterials. Table S1 (ESI†) lists the reported In-based halides. Generally, colloidal nanomaterials with small dimensions can be synthesized using a hot-injection method and the ligand-assisted reprecipitation (LARP) method. The synthesis of nanocrystals (NCs) with a uniform particle size distribution *via* the hot-injection method requires precise control of the injection temperature, precursor concentration, ratio of surfactants to precursors and reaction time. In our previous work, we synthesized Cs<sub>3</sub>InBr<sub>6</sub> nanomaterials with a hollow structure using the hot-injection method.<sup>27</sup> Limited by the synthesis conditions, the prepared hollow Cs<sub>3</sub>InBr<sub>6</sub> NCs have a larger size (above 20 nm) and are easily agglomerated in solution, which is not conducive to the formation of dense films during the manufacturing process of light-emitting devices. In addition, the hollow Cs<sub>3</sub>InBr<sub>6</sub> NCs have more Br vacancy defects, resulting in a lower PLQY. However, the synthesis of quantum dots (QDs) using the LARP method needs only the addition of a polar precursor solution in a suitable solvent to a

non-polar poor solvent at room-temperature (RT). This method is simpler and more controllable, and can synthesize quantum dot materials within 10 nm with a uniform size. In addition, the QD materials have a different surface state compared with the NCs materials, which is conducive to improving the PLQY.

Herein, we report the synthesis of 0D Cs<sub>3</sub>InX<sub>6</sub> (X = Cl, Br, or I) colloidal QDs *via* the modified LARP (m-LARP) technique, and a spectral tunability ranging from 397 to 535 nm was demonstrated using an anion exchange strategy. Importantly, the prepared Cs<sub>3</sub>InBr<sub>6</sub> QDs exhibited broadband blue emission from self-trapped excitons (STEs), with a PLQY as high as 46%, and the emission mechanism was studied further through density functional theory calculations and temperature-dependent PL measurements. Moreover, the as-synthesized Cs<sub>3</sub>InX<sub>6</sub> QDs show excellent stability compared with conventional lead halide perovskites. Finally, a WLED with the corresponding International Commission on Illumination (CIE) color coordinates (0.31,0.32) was manufactured using blue light-emitting Cs<sub>3</sub>InBr<sub>6</sub> QDs and yellow light-emitting (Ba,Sr)<sub>2</sub>SiO<sub>4</sub>:Eu<sup>2+</sup>. More importantly, the prepared WLED shows good long-term working stability with a half-life (*T*<sub>50</sub>) of 186 h at 29.1 °C, and a *T*<sub>50</sub> of 50 h even at 106.9 °C.

## Results and discussion

In our work, non-toxic Cs<sub>3</sub>InX<sub>6</sub> QDs were synthesized *via* the m-LARP method at RT. In the synthesis of Cs<sub>3</sub>InBr<sub>6</sub>, InBr<sub>3</sub>, CsBr and oleylamine (OAm) were dissolved in *N,N*-dimethylformamide (DMF) or dimethyl sulfoxide (DMSO) with vigorous stirring to form a clear precursor solution, as schematically illustrated in Fig. 1a. Then, the precursor solution was swiftly injected into the anti-solvent toluene to form the Cs<sub>3</sub>InBr<sub>6</sub> QD solution, where a small amount of oleic acid (OA) was incorporated to control the crystallization of the Cs<sub>3</sub>InBr<sub>6</sub> QDs. The OAm/OA system has been widely used in the synthesis of colloidal QDs, owing to its positive effects on reducing the agglomeration and stabilizing the colloidal QD solution.<sup>28–30</sup>

In order to improve the luminescence efficiency of the Cs<sub>3</sub>InBr<sub>6</sub> QDs, a series of comparable experiments with different precursor concentrations was performed. At an optimized molar ratio of 3 : 1.5 for CsBr/InBr<sub>3</sub>, a maximum PLQY of about 46% was achieved, as seen in Fig. S1 and S2 (ESI†). The crystal structure of Cs<sub>3</sub>InBr<sub>6</sub> with the cubic space group of *Fm* $\bar{3}$ *m* is shown in Fig. 1b in which the [InBr<sub>6</sub>]<sup>3–</sup> units are completely separated by the surrounding Cs<sup>+</sup> cations, forming the 0D structural motif. In this symmetric unit, the In ions are octahedrally coordinated by six halogen anions to produce [InBr<sub>6</sub>]<sup>3–</sup> anions. Note that this unique 0D structure of Cs<sub>3</sub>InBr<sub>6</sub> will result in a strong localized electronic distribution. Therefore, the photoexcited electrons and holes easily form excitons due to a strong Coulombic effect. Thus, a large exciton binding energy and an appreciable PLQY can be expected. Fig. 1c presents the typical X-ray diffraction (XRD) pattern of the Cs<sub>3</sub>InBr<sub>6</sub> QDs, where the observed diffraction peaks (top) match very well with the theoretically calculated data (bottom),

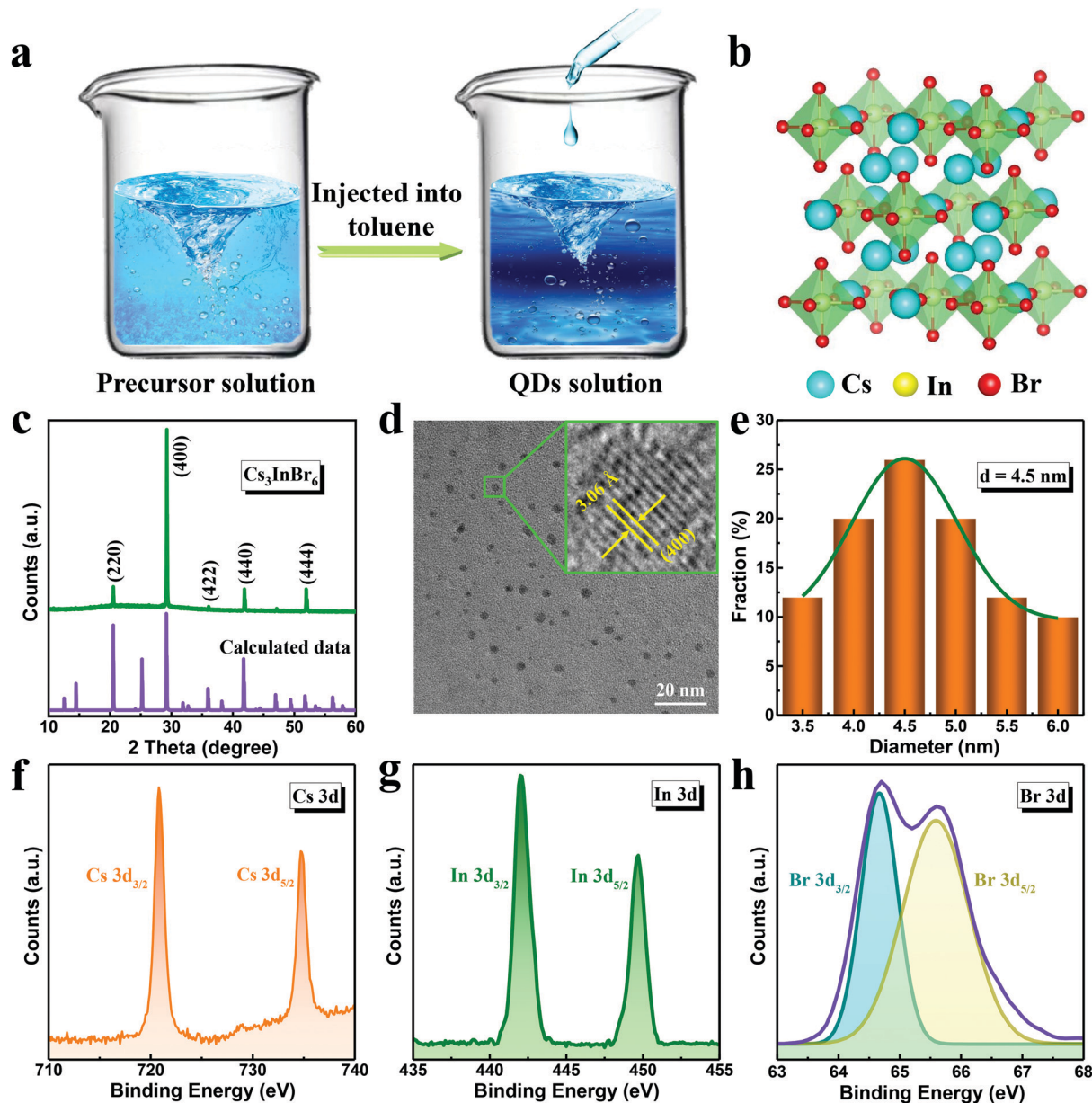


**Fig. 1** (a) Schematic illustration of the synthesis of  $\text{Cs}_3\text{InBr}_6$  QDs using the m-LARP technique. (b) Crystal structure and (c) XRD patterns of the  $\text{Cs}_3\text{InBr}_6$  QDs. (d) TEM image of the  $\text{Cs}_3\text{InBr}_6$  QDs. The inset shows a HRTEM image of the  $\text{Cs}_3\text{InBr}_6$  QD. (e) Size distribution of the  $\text{Cs}_3\text{InBr}_6$  QDs. High-resolution XPS spectra of (f) Cs 3d, (g) In 3d, and (h) Br 3d for the  $\text{Cs}_3\text{InBr}_6$  QDs.

confirming a pure cubic  $\text{Cs}_3\text{InBr}_6$  phase (space group  $Fm\bar{3}m$ ,  $a = b = c = 11.63 \text{ \AA}$ ,  $\alpha = \beta = \gamma = 90^\circ$ ). The transmission electron microscopy (TEM) image shows that the  $\text{Cs}_3\text{InBr}_6$  QDs have a quasi-spherical morphology with an average size of 4.5 nm (Fig. 1d). The inset displays the high-resolution TEM (HRTEM) image of the QD in which clear lattice fringes with a  $d$ -spacing of 3.06 Å are observed, corresponding to the (400) crystal plane. It is worth noting that the  $\text{Cs}_3\text{InBr}_6$  QDs still show obvious lattice fringes without degradation after 120 s of continuous irradiation under the electron beam (Fig. S3, ESI<sup>†</sup>), which indicates that the QDs have good stability under electron beam irradiation. Moreover, in order to determine the chemical composition and valence states of the  $\text{Cs}_3\text{InBr}_6$  QDs, the X-ray

photoelectron spectroscopy (XPS) measurements were performed. From the total XPS spectrum shown in Fig. S4 (ESI<sup>†</sup>), one can see that the signals of Cs, In, and Br can be detected, and the corresponding molar ratio is 27.13 : 9.97 : 62.9, close to the stoichiometry of  $\text{Cs}_3\text{InBr}_6$ . The high-resolution XPS spectra of the three elements are shown in Fig. 1f–h. Two peaks at 734.7 and 720.8 eV correspond to the spin-orbit of Cs 3d<sub>5/2</sub> and Cs 3d<sub>3/2</sub>, respectively. For In 3d spectrum, two peaks at 449.7 and 442.0 eV were observed, derived from the In 3d<sub>5/2</sub> and In 3d<sub>3/2</sub>, respectively, indicating the valence state of trivalent In. The binding energies of Br 3d at 64.6 and 65.6 eV can be assigned to the Br 3d<sub>3/2</sub> and Br 3d<sub>5/2</sub> levels originating from the Br<sup>−</sup> in  $\text{Cs}_3\text{InBr}_6$ . An additional observation is that the atomic ratio of

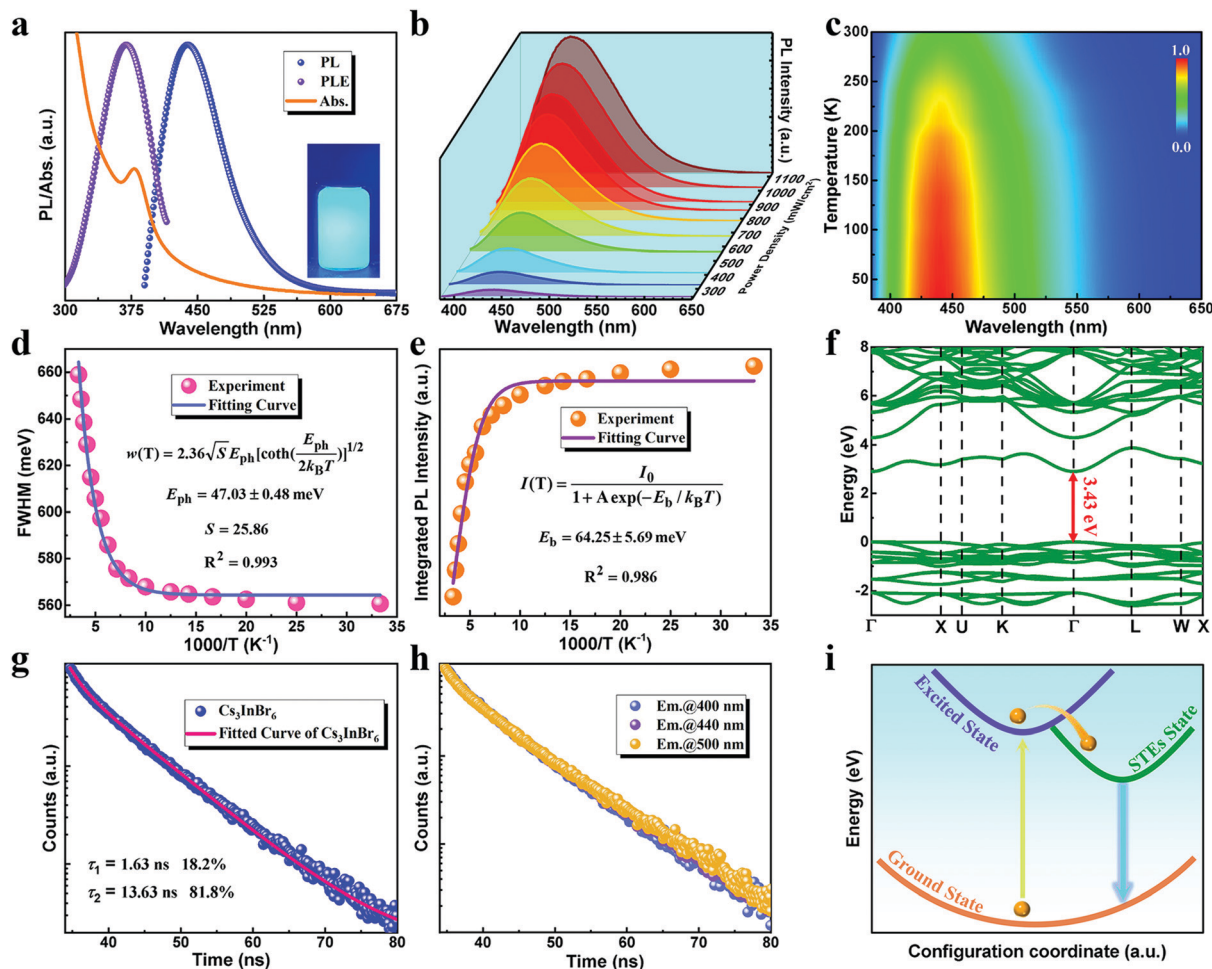


Fig. 2 (a) PLE, PL and absorption spectra of the  $\text{Cs}_3\text{InBr}_6$  QDs. The inset shows the luminescence photo of the  $\text{Cs}_3\text{InBr}_6$  colloidal QD solution excited by 365 nm UV light. (b) PL spectra obtained with different excitation power densities. (c) Pseudocolor maps of temperature-dependent PL spectra. (d) FWHM and (e) integrated PL intensity of the  $\text{Cs}_3\text{InBr}_6$  QDs as a function of the reciprocal temperature. (f) Calculated band structure of  $\text{Cs}_3\text{InBr}_6$ . (g) Time-resolved PL decay of the  $\text{Cs}_3\text{InBr}_6$  QDs. (h) Time-resolved PL decay of the  $\text{Cs}_3\text{InBr}_6$  QDs at different emission wavelengths. (i) Schematic of the photophysical processes in  $\text{Cs}_3\text{InBr}_6$  QDs.

Br/In obtained by XPS analysis is about 6.31 : 1, which is slightly higher than the stoichiometric ratio, indicating the Br-rich surface of the  $\text{Cs}_3\text{InBr}_6$  QDs.

To study the optical properties of the as-prepared  $\text{Cs}_3\text{InBr}_6$  colloidal QDs, the absorption, PL excitation (PLE) and PL spectra were therefore measured. As shown in Fig. 2a, the exciton absorption peak and emission peak of the  $\text{Cs}_3\text{InBr}_6$  QDs are located at 370 nm and 440 nm, respectively, showing a large Stokes shift of 70 nm and an FWHM of 80 nm. Such a large Stokes shift of the  $\text{Cs}_3\text{InBr}_6$  colloidal QDs helps to reduce the photon self-absorption capacity, making the QDs suitable as a down-conversion phosphor for lighting applications. The inset shows the luminescence photo of the  $\text{Cs}_3\text{InBr}_6$  QD solution under a 365 nm UV lamp, which exhibits blue emission, and the PLQY measured using an integrating sphere is as high as 46% (Fig. S2, ESI<sup>†</sup>).

Generally, the broadband emission feature shows that the emission is caused by STE, which is related to the soft lattice properties of the material. Such emission behavior has been

frequently observed in alkali halides and low-dimensional metal halide perovskite materials.<sup>31–34</sup> It is important to note that other possibilities could also explain this broadband emission behavior, including the radiative recombination of excitons combined with defects such as isoelectronic impurities, although large amounts of impurities are required to induce such emissions.<sup>35</sup> Excitation-power-dependent PL measurements can more effectively help us to distinguish the emission related to excitons or permanent material defects. Fig. 2b and Fig. S5 (ESI<sup>†</sup>) show that the integrated PL intensity of the 0D  $\text{Cs}_3\text{InBr}_6$  colloidal QDs increases with an increase of the excitation power density, with a slope of  $1.92 \pm 0.04$ , indicating the exciton transitions and ruling out the possibility of permanent defect-related emission.<sup>36</sup> In addition, the wavelength-dependent PLE and PL spectra indicate that the PLE and PL spectra show nearly identical spectral shapes and peak positions at different emission and excitation wavelengths (Fig. S6, ESI<sup>†</sup>), suggesting that the blue emission originates from relaxation of the same excited state.<sup>37</sup> It is generally accepted that the emission and absorption of phonons

can change the energy of the transitions and broaden the steep transition into broadband emission in other ways, which largely depends on the strength of the electron–phonon coupling. The electron–phonon interactions cause a local deformation of the lattice, called a polaron, which couples with carriers and increases their effective masses. In the case of a strong coupling, the polarons bind the carriers to the lattice sites (called self-trapping) and significantly broaden the optical spectrum.<sup>35</sup>

In addition, in order to gain insight into the exciton–phonon interaction and STE dynamics, we performed a temperature-dependent PL test. The pseudocolor diagram of the PL spectrum of the Cs<sub>3</sub>InBr<sub>6</sub> colloidal QDs shown in Fig. 2c confirms that there is no peak characteristic of the free exciton zero-phonon line at low temperature, which may be caused by the inability of free carriers to recombine directly due to the carrier trapping.<sup>38</sup> The broad and skewed shape of the PL peaks at low temperatures can be attributed to the strong electron–phonon coupling, which leads to charge localization and emission of phonons that alter the energy of the emitted photon.<sup>35</sup> Besides, the PL peak position of the Cs<sub>3</sub>InBr<sub>6</sub> colloidal QDs undergoes a continuous blue shift (~5 nm) with increasing temperature, which agrees well with previously reported perovskites, for example, CsPbBr<sub>3</sub>, Cs<sub>3</sub>Bi<sub>2</sub>Br<sub>9</sub>, and Cs<sub>3</sub>Sb<sub>2</sub>Br<sub>9</sub>, which is caused by the strong electron–phonon interaction, mainly from longitudinal optical phonon coupling.<sup>39–42</sup> In addition, Toyozawa's theory was used to model the temperature-dependence of the FWHM (denoted as  $w(T)$ ) of the emission peak.<sup>43</sup> This modified theory uses a configuration to model the emission broadening caused by the electron–phonon interaction,<sup>44</sup>

$$w(T) = 2.36\sqrt{S}E_{\text{ph}} \left[ \coth\left(\frac{E_{\text{ph}}}{2k_{\text{B}}T}\right) \right]^{1/2} \quad (1)$$

where  $S$  is the Huang–Rhys electron–phonon coupling parameter, and  $E_{\text{ph}}$  is the effective phonon energy. Among these,  $S$  characterizes the strength of the electron–phonon coupling ( $S < 1$ , weak coupling structure;  $1 < S < 5$ , heavy coupling structure; and  $S > 5$ , strong coupling structure).<sup>45</sup> According to eqn (1), the dependence of FWHM on the temperature was analyzed (Fig. 2d), yielding  $S = 25.86$  and the phonon energy  $E_{\text{ph}} = 47.03$  meV. Note that  $S = 25.86$  is equivalent to the value of alkali metal halides, indicating that the electron–phonon coupling in the Cs<sub>3</sub>InBr<sub>6</sub> QDs is very strong.<sup>46,47</sup> The strong electron–phonon coupling induces small polarons in the crystal lattice, thereby locally trapping the charge carriers, subsequently causing the formation of STEs.<sup>48–54</sup> Moreover, the exciton binding energy ( $E_{\text{b}}$ ) of the Cs<sub>3</sub>InBr<sub>6</sub> QDs can be obtained by fitting the integrated PL intensity at various temperatures,

$$I(T) = \frac{I_0}{1 + A \exp(-E_{\text{b}}/k_{\text{B}}T)} \quad (2)$$

where  $I_0$  is the integrated PL intensity at 0 K and  $k_{\text{B}}$  is the Boltzmann constant. According to the fitting analysis (Fig. 2e), a large exciton binding energy of about 64.25 meV was achieved. This is easily understandable because of the 0D structural nature of Cs<sub>3</sub>InBr<sub>6</sub>, where each [InBr<sub>6</sub>]<sup>3−</sup> octahedron is isolated, and thereby the exciton's localization is strengthened. Such a high

exciton binding energy ensures the survival of excitons well above RT and their high-rate recombination, and also indicates that the broadband emission of the Cs<sub>3</sub>InBr<sub>6</sub> colloidal QDs comes from the recombination of excitons.<sup>55,56</sup>

Generally speaking, low-dimensional metal halides with STEs emission characteristics have the quantum confinement effects.<sup>57</sup> The Cs<sub>3</sub>InBr<sub>6</sub> has a direct bandgap of 3.43 eV with the conduction band minimum (CBM) and the valence band maximum (VBM) being located at the  $\Gamma$  point (Fig. 2f), higher than the measured value (3.07 eV) shown in Fig. S7 (ESI<sup>†</sup>), mainly because DFT always overestimates the bandgap values.<sup>58</sup> One can observe that the electron energy band structure shows a flat highest valence band, indicating that this 0D compound has a heavy hole effective mass and strong quantum confinement characteristics.<sup>59</sup> The predicted density of states (PDOS) of Cs<sub>3</sub>InBr<sub>6</sub> was also calculated. The VBM is mainly contributed by the In 4d orbitals and some Br 5p orbitals, whereas the CBM is composed of In 5s and Br 5p orbitals (Fig. S8, ESI<sup>†</sup>). Cs<sup>+</sup> as the positive charge intermediate lattice makes little contribution to light absorption and emission. Therefore, the [InBr<sub>6</sub>]<sup>3−</sup> octahedron determines the photophysical properties of the compound Cs<sub>3</sub>InBr<sub>6</sub>. Although Cs<sub>3</sub>InBr<sub>6</sub> has a dispersive conduction band, the excitons prefer localization due to local structural distortion of the [InBr<sub>6</sub>]<sup>3−</sup> octahedron under light excitation, resulting in a strong exciton-related emission.

Furthermore, to study the exciton recombination dynamics of the Cs<sub>3</sub>InBr<sub>6</sub> QDs, we performed time-resolved PL measurements. The PL decay curve of the Cs<sub>3</sub>InBr<sub>6</sub> QDs can be well fitted by a double exponential function, as shown in Fig. 2g, producing a short lifetime  $\tau_1 = 1.63$  ns (18.2%) and a long lifetime  $\tau_2 = 13.63$  ns (81.8%), suggesting the presence of two different types of STE emission behavior. Among them, the short-lived process may originate from the spin singlet, and the long-lived process may originate from the spin triplet. The lifetime of the Cs<sub>3</sub>InBr<sub>6</sub> QDs has the same order of magnitude (ns) as the reported perovskites Cs<sub>3</sub>BiCl<sub>6</sub>,  $\beta$ -Cs<sub>3</sub>Cu<sub>2</sub>Cl<sub>5</sub>, and Rb<sub>7</sub>Bi<sub>3</sub>Cl<sub>16</sub>, which have STE characteristics,<sup>60–62</sup> whereas it is smaller than those of the reported In-based halide single crystals.<sup>22–25</sup> For Cs<sub>3</sub>InBr<sub>6</sub>, [InBr<sub>6</sub>]<sup>3−</sup> is a regular octahedron composed of six identical Br<sup>−</sup> ions, resulting in a smaller lattice distortion during optical excitation, which has a great effect on the emission and restructuring time of the STEs. That is, the degree of Jahn–Teller distortion determines the strength of the emission and the length of the restructuring time of the STEs.<sup>63–66</sup> In addition, the time-resolved PL decay curves of the Cs<sub>3</sub>InBr<sub>6</sub> QDs monitored at different emission wavelengths are comparable (Fig. 2h), which further indicates that the emission comes from the same emission center. The configuration coordinate diagram in Fig. 2i illustrates the STE dynamic processes of the Cs<sub>3</sub>InBr<sub>6</sub> QDs. Because of the 0D nature of Cs<sub>3</sub>InBr<sub>6</sub>, which features strong electron–phonon coupling, excited carriers become highly localized. As a result, the excitons generated by the photoexcitation are immediately trapped by the lattice deformations upon formation, forming emissive STE states in equilibrium.

Furthermore, the photophysical properties of the Cs<sub>3</sub>InX<sub>6</sub> QDs can be adjusted using a simple halogen anion exchange

method. As shown in Fig. 3a, the synthesized  $\text{Cs}_3\text{InCl}_6$  and  $\text{Cs}_3\text{InI}_6$  QDs have the same 0D structure as that of  $\text{Cs}_3\text{InBr}_6$ , and the measured XRD patterns match their theoretical values very well (Fig. S9, ESI<sup>†</sup>). Fig. 3b and c present the corresponding TEM images of  $\text{Cs}_3\text{InCl}_6$  and  $\text{Cs}_3\text{InI}_6$  QDs, which all maintained the quasi-spherical shape with uniform distribution, and their average sizes are about 2.1 and 2.8 nm, respectively (Fig. S10, ESI<sup>†</sup>).

The insets show the HRTEM images of  $\text{Cs}_3\text{InCl}_6$  and  $\text{Cs}_3\text{InI}_6$  QDs, where the observed lattice fringes correspond to the cubic  $\text{Cs}_3\text{InX}_6$  structure. Fig. 3d displays a series of absorption and emission spectra of the  $\text{Cs}_3\text{InX}_6$  QDs obtained by controlling the anion exchange reaction process, and a regular emission wavelength change from 397 nm ( $\text{Cs}_3\text{InCl}_6$ ) to 535 nm ( $\text{Cs}_3\text{InI}_6$ ) was achieved, where all these mixed-halide QDs maintain the broadband emission characteristics. Analogously, the absorption edges of all the resulting  $\text{Cs}_3\text{InX}_6$  QDs present a red-shift trend from  $\sim 320$  nm ( $\text{Cs}_3\text{InCl}_6$ ) to  $\sim 505$  nm ( $\text{Cs}_3\text{InI}_6$ ). In addition, the PLQY values of all the  $\text{Cs}_3\text{InX}_6$  QDs were measured, and the detailed data can be found in Table 1.

In order to evaluate the applicability of the obtained  $\text{Cs}_3\text{InX}_6$  QDs in actual optoelectronic devices, we studied the influence of the external environment on the  $\text{Cs}_3\text{InX}_6$  QDs in which the

$\text{Cs}_3\text{InBr}_6$  QDs were taken as an example and the emission intensity was normalized for comparison. First, we studied the photostability of the  $\text{Cs}_3\text{InBr}_6$  QDs by continuously illuminating the QD solution using a 365 nm UV lamp with a distance of 10 cm. As shown in Fig. 4a and Fig. S11 (ESI<sup>†</sup>), the QD solution shows an obvious photoactivation effect within the first 8 h, and then the PL intensity decreases by 21.5% after 100 h of illumination, without any change in the spectral shape and peak position. Note that the photoactivation phenomenon has also been observed in other QDs systems,<sup>21</sup> which may be caused by the smoothness of the QDs and the elimination of dangling bonds or other surface defects. The insets to Fig. 4a show photographs of the  $\text{Cs}_3\text{InBr}_6$  QD solution after different illumination periods, and bright blue emission can still be observed after continuous illumination for 100 h. In general, lead halide perovskites will decompose easily once exposed to a high-humidity environment owing to the hygroscopic halide salts. In our case, to evaluate the moisture stability of the  $\text{Cs}_3\text{InBr}_6$  QDs, an aggressive water treatment process was therefore carried out, and 300  $\mu\text{L}$  of deionized water was added to the QD solution, sonicated for 1 min to make the deionized water uniformly dispersed in the QD solution. As shown in Fig. 4b, the  $\text{Cs}_3\text{InBr}_6$  QDs experience a rather slow fluorescence

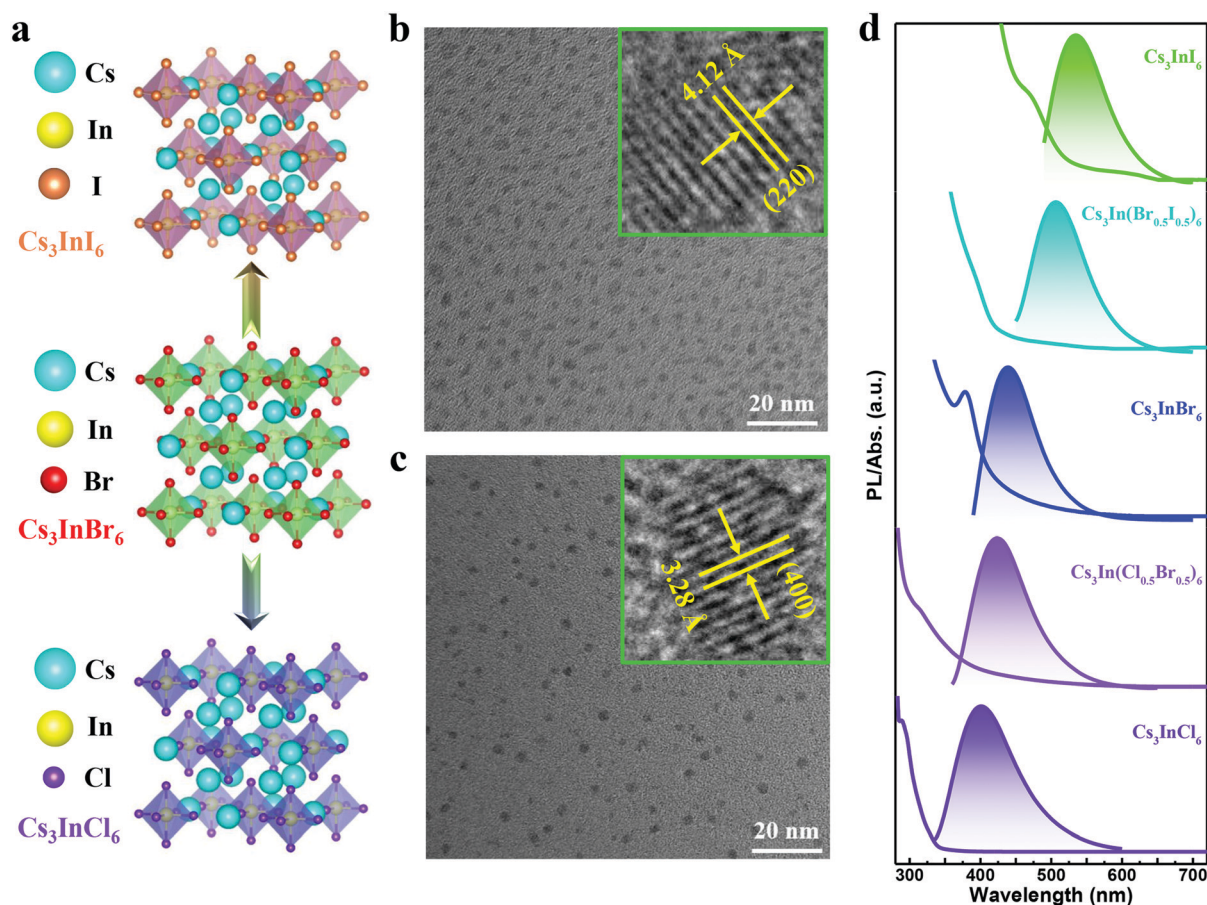


Fig. 3 (a) Crystal structures of  $\text{Cs}_3\text{InX}_6$  ( $X = \text{Cl}, \text{Br}, \text{or I}$ ). TEM images of (b)  $\text{Cs}_3\text{InCl}_6$  and (c)  $\text{Cs}_3\text{InI}_6$ . The insets show the corresponding HRTEM images of the  $\text{Cs}_3\text{InCl}_6$  and  $\text{Cs}_3\text{InI}_6$  QDs. (d) Composition-tunable absorption and PL spectra of the  $\text{Cs}_3\text{InX}_6$  QDs.

Table 1 Summary of PLQYs and emission peaks for the Cs<sub>3</sub>InX<sub>6</sub> QDs

QDs	Emission peak (nm)	FWHM (nm)	Stokes shift (nm)	PLQY (%)
Cs <sub>3</sub> InCl <sub>6</sub>	397	98	107	24
Cs <sub>3</sub> In(Cl <sub>0.5</sub> Br <sub>0.5</sub> ) <sub>6</sub>	424	89	113	6
Cs <sub>3</sub> InBr <sub>6</sub>	440	80	70	46
Cs <sub>3</sub> In(Br <sub>0.5</sub> I <sub>0.5</sub> ) <sub>6</sub>	507	87	103	2
Cs <sub>3</sub> InI <sub>6</sub>	535	87	75	16

quenching process after the addition of water. At the end of a long-term storage period of 48 h, PL intensity only decays by 14%, which is much superior to that of CsPbBr<sub>3</sub> QDs that are almost “dead” within tens of minutes.<sup>42</sup> In addition, we also tested the stability of the Cs<sub>3</sub>InBr<sub>6</sub> QD film under 365 nm UV irradiation and a high-humidity environment (70–80% humidity). As shown in Fig. S12 (ESI<sup>†</sup>), the PL spectral shape of the QD film almost did not change and the PL intensity was only attenuated by 16.2% after continuous irradiation for 70 h in a high-humidity environment. The insets show that the bright-blue emission can be observed after continuous treatment of the QD film for 70 h. Even when exposed to a high-humidity environment in the open air (20–35 °C, 50–60%) for 60 days, the Cs<sub>3</sub>InBr<sub>6</sub> QDs can still maintain their phase purity without decomposition, as shown in Fig. S13 (ESI<sup>†</sup>).

The thermal quenching behavior is an important indicator for evaluating the potential of luminescent materials for LED applications. Therefore, we investigated the thermal stability of the Cs<sub>3</sub>InBr<sub>6</sub> QDs by performing temperature-dependent PL tests.

The PL intensity of Cs<sub>3</sub>InBr<sub>6</sub> QDs is gradually quenched owing to heat-induced non-radiative recombination as the temperature is increased, as shown in Fig. 4c. When the temperature was gradually increased to 100 °C, the PL intensity decayed to 70% of the initial value, although the initial spectral shape was maintained. Excitingly, after the temperature was lowered to RT (20 °C), the PL intensity of the Cs<sub>3</sub>InBr<sub>6</sub> QDs was restored to the original level, as shown in Fig. 4d. Even after 15 successive heating/cooling cycles, above 97% of the initial PL intensity was preserved (Fig. S14, ESI<sup>†</sup>), which shows that the Cs<sub>3</sub>InBr<sub>6</sub> QDs have good heat resistance. The above observations show that the 0D Cs<sub>3</sub>InBr<sub>6</sub> QDs have significant thermal tolerance, which opens up huge opportunities for manufacturing high-performance optoelectronic devices. Furthermore, we heated the Cs<sub>3</sub>InBr<sub>6</sub> QD film sample at 100 °C for 150 h and continuously monitored its emission performance. From the pseudocolor map shown in Fig. 4e, one can see that the PL intensity shows a decay of ~20%. It can be understood that the heat quenching effect will be intensified with the extension of heating time in long-term heating tests. Despite this, the thermal stability of the Cs<sub>3</sub>InBr<sub>6</sub> QDs is significantly better than that of other reported perovskite QDs materials such as CsPbBr<sub>3</sub>, Cs<sub>3</sub>Bi<sub>2</sub>Br<sub>9</sub>, Cs<sub>3</sub>Sb<sub>2</sub>Br<sub>9</sub>, *etc.*<sup>21,39–41</sup> Here, we believe that the superior thermal stability of the Cs<sub>3</sub>InBr<sub>6</sub> QD depends on its 0D structural dimension, which is beneficial for increasing its inherent structural stability. Besides, 0D Cs<sub>3</sub>InBr<sub>6</sub> has a shorter metal–Br bond length than other perovskite systems, as illustrated in Fig. 4f, thus increasing the stiffness of the [InBr<sub>6</sub>]<sup>3-</sup> octahedron. The experimental results

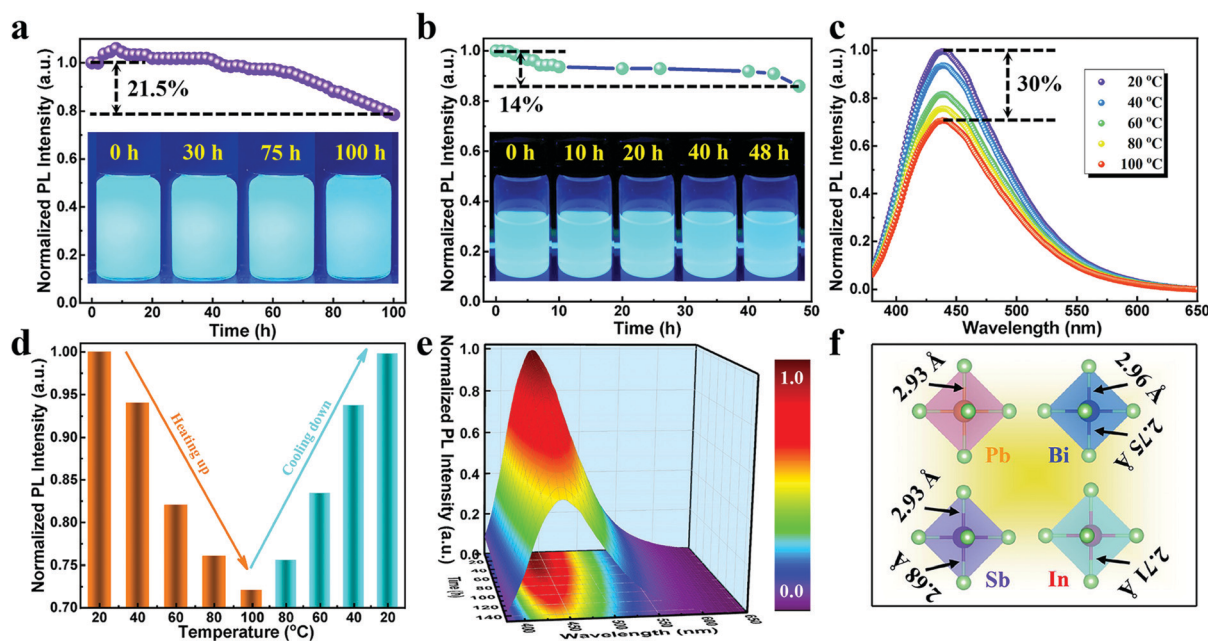


Fig. 4 (a) Photostability test of the Cs<sub>3</sub>InBr<sub>6</sub> QDs under UV light irradiation (365 nm, 8 W) for 100 h. The insets show photographs of the Cs<sub>3</sub>InBr<sub>6</sub> QD solution for different UV irradiation times. (b) Stability test of the Cs<sub>3</sub>InBr<sub>6</sub> QD solution against water corrosion (300 μL of deionized water was added to 3 mL of the Cs<sub>3</sub>InBr<sub>6</sub> QD toluene solution). The insets show photographs of the Cs<sub>3</sub>InBr<sub>6</sub> QD solution captured at different time periods after adding the deionized water. (c) PL spectral evolution of the Cs<sub>3</sub>InBr<sub>6</sub> QD film at different measurement temperatures. (d) Comparison of the normalized PL intensities of the Cs<sub>3</sub>InBr<sub>6</sub> QDs over one heating/cooling cycle. (e) Long-term thermal stability test of the Cs<sub>3</sub>InBr<sub>6</sub> QD film at a high temperature of 100 °C. (f) Comparison of the octahedral structures of CsPbBr<sub>3</sub>, Cs<sub>3</sub>Bi<sub>2</sub>Br<sub>9</sub>, Cs<sub>3</sub>Sb<sub>2</sub>Br<sub>9</sub>, and Cs<sub>3</sub>InBr<sub>6</sub>.

altogether indicate the remarkable stability of such a 0D Cs<sub>3</sub>InX<sub>6</sub> QD system, making it suitable as an environmentally friendly light emitter that is suitable for the practical applications under harsh conditions.

To demonstrate the application potential of non-toxic cesium indium halide QDs in the field of lighting, a WLED was prepared by combining bright-blue-emissive Cs<sub>3</sub>InBr<sub>6</sub> QDs with the yellow-emissive (Ba,Sr)<sub>2</sub>SiO<sub>4</sub>:Eu<sup>2+</sup> phosphor, cured and packaged on a 365 nm LED chip. As seen in Fig. 5a and c, the WLED presents bright white light under a driving current of 6 mA, and shows a good color discrimination ability with the CIE color coordinates at (0.31,0.32). Fig. 5b displays the typical emission spectrum of the WLED, and the PL peaks corresponding to each phosphor can be observed at 440 and 556 nm, respectively. With the increase of the driving current, both emission components increase simultaneously (Fig. 5d), and the resulting CIE color coordinates and corresponding color temperature (CCT) show almost no change (Fig. S15, ESI†), which means that the two phosphors show no saturation under

strong current excitation, and the emission intensities and current values of the two phosphors increase linearly, even at a high working current. In real life, light sources must work at high-injection level, and thus the influence of undesired heating effects has to be considered. We first measured the operating temperature of the WLED at various driving currents (6, 100, 200, and 300 mA) using an infrared camera. As shown in Fig. 5e, as the driving current is increased, the surface operating temperature of the WLED gradually increases, reaching a maximum value of 106.9 °C at 300 mA. Benefiting from the non-contact device configuration of the WLED, the down-conversion phosphor layer is separated from the p-n junction of the bottom excited LED. Due to the considerable distance between the phosphor and the LED chip, the heat released by the LED chip is unlikely to reach the upper phosphor. Therefore, even when a high driving current is applied for 10 h, the surface temperature of WLED does not increase further, as shown in Fig. 5f, which suggests that the WLED is able to maintain a constant temperature under a high driving current. Therefore, we evaluated

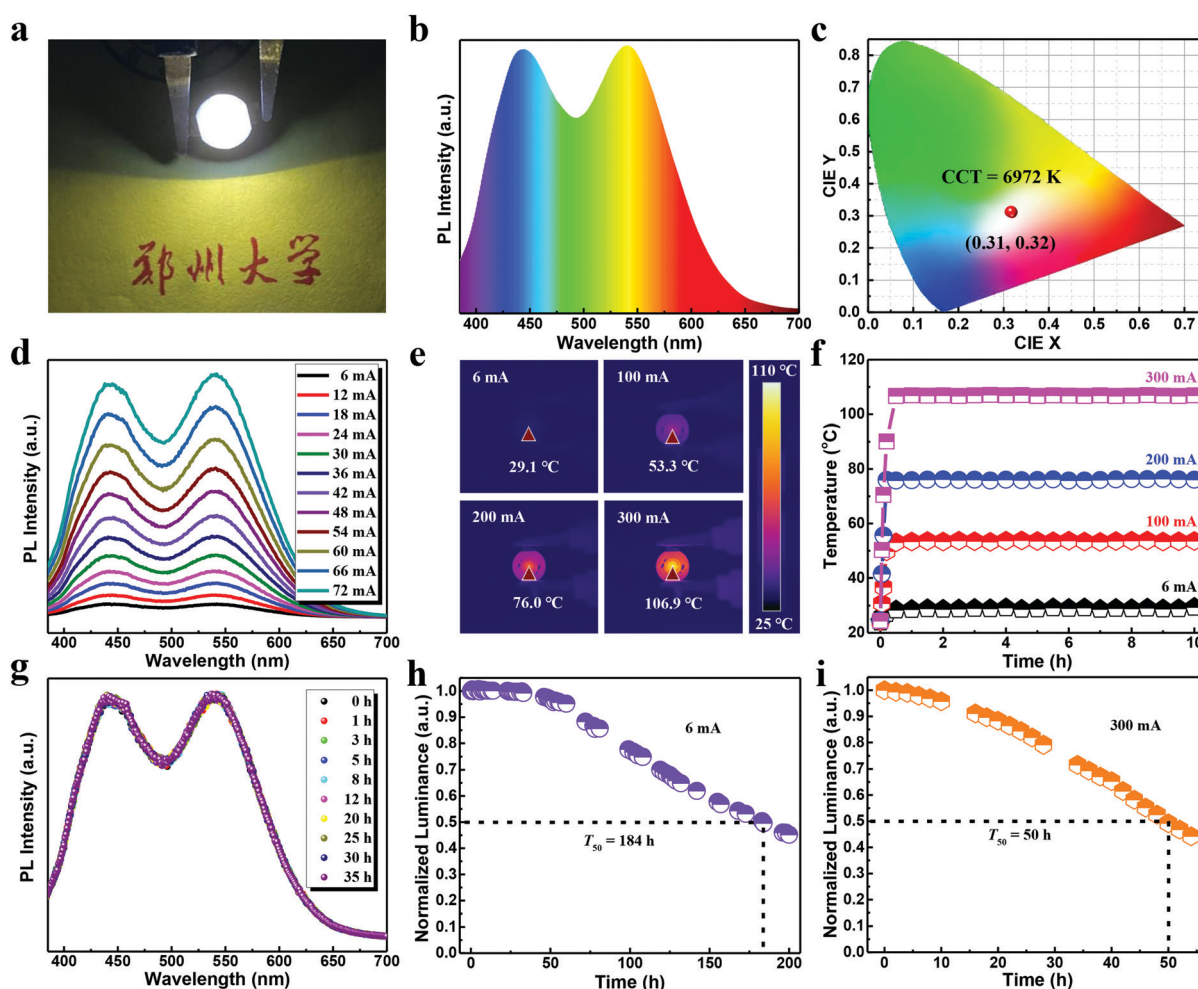


Fig. 5 (a) Photograph of the working WLED at a driving current of 6 mA. (b) Emission spectrum and (c) CIE color coordinates of the WLED. (d) Emission spectra of the WLED in the current range of 6–72 mA. (e) Thermographs of the WLED in the driving current range of 6–300 mA. (f) Temperature change of the WLED as a function of running time under different driving currents of 6, 100, 200 and 300 mA, respectively. (g) Emission spectra of the WLED at different running periods. The emission intensities of the WLED evolving with the operating time at (h) 6 mA and (i) 300 mA driving currents, respectively.

the long-term operating stability of the studied WLED after the temperature of the device reached a steady state at different driving current levels, and extracted its  $T_{50}$  value. As shown in Fig. 5g, at a low current level of 6 mA, the emission performance of the WLED shows no change for a continuous working period of 35 h. By extending the running time of the device to 200 h, we can deduce a long  $T_{50}$  value of about 184 h, as seen in Fig. 5h, which is much longer than that of traditional lead-based perovskite WLEDs.<sup>8,42,67</sup> As the driving current was increased to 100 mA, 200 mA and 300 mA (Fig. S16, ESI† and Fig. 5i), the  $T_{50}$  value showed a decreasing trend; specifically, the values of  $T_{50}$  obtained are 116, 80, and 50 h, respectively. This is easily understandable because a higher driving current of the LED chip means stronger UV light excitation and more heat generation, which altogether damage the  $\text{Cs}_3\text{InBr}_6$  QDs to a greater extent. Despite this, such a WLED still has a  $T_{50}$  of up to 50 h at a high temperature of 106.9 °C, which highlights the excellent photo- and thermal-stability of the  $\text{Cs}_3\text{InBr}_6$  QD phosphor, demonstrating its potential in solid-state lighting technology applications.

## Conclusions

In summary, we have successfully synthesized non-toxic 0D  $\text{Cs}_3\text{InX}_6$  QDs using the modified LARP method, and the emission wavelength was readily tunable over the spectral range of 397–535 nm through an anion exchange strategy. For the blue-emissive  $\text{Cs}_3\text{InBr}_6$  QDs, a high PLQY of 46% was achieved. The broadband emission feature can be ascribed to the formation of self-trapped excitons owing to the strong electron–phonon coupling of  $\text{Cs}_3\text{InBr}_6$  as evidenced by first-principles calculations and temperature-dependent PL measurements. Thanks to the excellent stability of the  $\text{Cs}_3\text{InBr}_6$  QDs, a stable WLED was produced using blue-emissive  $\text{Cs}_3\text{InBr}_6$  QD powder as a color-conversion phosphor, and produced a record  $T_{50}$  of 186 h at a 6 mA (29.1 °C) operating current. Even in high current mode of 300 mA (106.9 °C), the device can operate normally with a  $T_{50}$  of 50 h. Coupled with an eco-friendly and a simple synthesis process, the non-toxic and stable  $\text{Cs}_3\text{InBr}_6$  QDs can be regarded as a promising alternative to blue light emitters, suggesting their potential for applications in lighting fields.

## Experimental section

### Materials

CsBr ( $\geq 99.999\%$ ), CsCl ( $\geq 99.999\%$ ), CsI ( $\geq 99.99\%$ ),  $\text{InCl}_3$  ( $\geq 99.9\%$ ),  $\text{InBr}_3$  ( $\geq 99.9\%$ ),  $\text{InI}_3$  ( $\geq 99.9\%$ ), OA (90%), and OAm (90%) were purchased from Aladdin. DMF, DMSO, hexane, isopropanol, ethanol, and *n*-octane were purchased from Beijing Chemical Reagent Co., Ltd, China.

### Preparation of $\text{Cs}_3\text{InX}_6$ QDs

0.6 mmol of CsBr, 0.2 mmol of  $\text{InBr}_3$  and 200  $\mu\text{L}$  of OAm were dissolved in a mixed solution of 4 mL of DMF and 4 mL of DMSO. After that, under vigorous stirring at room temperature, 0.8 mL of the precursor solution was quickly injected into a

mixed solution of 5 mL of toluene and 1 mL of OA and stirred for 10 min. The product was then centrifuged at 10 000 rpm for 5 min to discard the precipitate containing large particles and the supernatant was kept for further use and characterization. The solid powder of  $\text{Cs}_3\text{InBr}_6$  QDs was obtained by rotary evaporation of the residual organic solvents at 85 °C. The mixed-halide perovskites  $\text{Cs}_3\text{InCl}_6$ ,  $\text{Cs}_3\text{In}(\text{Cl}_{0.5}\text{Br}_{0.5})_6$ ,  $\text{Cs}_3\text{In}(\text{Br}_{0.5}\text{I}_{0.5})_6$ , and  $\text{Cs}_3\text{InI}_6$  were fabricated: 0.3 mmol of CsCl or CsI was dissolved in 10 mL and 4 mL of DMSO solution, respectively. Then, 1 mL or 300  $\mu\text{L}$  of CsCl or CsI solution was added to the  $\text{Cs}_3\text{InBr}_6$  QDs solution and stirred for 10 min.

### Fabrication of the WLED devices

The  $\text{Cs}_3\text{InBr}_6$  QD powder and yellow-emissive  $(\text{Ba,Sr})_2\text{SiO}_4:\text{Eu}^{2+}$  phosphor were mixed with PDMS (PDMS A and PDMS B (A : B = 10 : 1, wt%)) to prepare a homogeneous latex. The resulting mixture was then heated at 60 °C for 1 h to degas. After that, the mixture was added dropwise onto a UV LED chip and then thermally cured for 3 h at 120 °C in an oven.

### Characterization of materials

The microstructure of the  $\text{Cs}_3\text{InX}_6$  QDs was characterized using a JEM-3010 instrument (JEOL). XRD of the  $\text{Cs}_3\text{InX}_6$  QDs was studied using a Panalytical X'Pert Pro instrument. Samples were drop-cast onto a quartz substrate forming a thin film. XPS data of the  $\text{Cs}_3\text{InBr}_6$  QDs were obtained using a SPECS XR50 instrument. Absorption spectra were obtained using a Shimadzu UV-3150 spectrophotometer. Samples were dispersed in toluene for measurements. PL spectra of the samples were obtained using a spectrophotometer (Horiba; Fluorolog-3). Time-resolved PL attenuation curves were obtained using a Pulsed Nano LED (Horiba; 370 nm) measurement system. The PLQYs of the  $\text{Cs}_3\text{InX}_6$  QD solutions were obtained using an integrating sphere (Horiba; Quanta- $\phi$ ) test system. A fluorescence spectrometer equipped with a closed-loop helium cryostat (Jannis CCS-100) and a digital temperature controller (LakeShore-325) was used to obtain the temperature-dependent PL spectra.

### WLED device measurements

The emission performance and operation stability of the WLEDs were measured using a Keithley 2400 source meter and a PR650 Spectra Scan spectrophotometer (Photo Research) in ambient air.

### Theoretical calculations

First-principles calculations were carried out based on DFT, using the plane wave pseudopotential method implemented in the Vienna *ab initio* simulation package (VASP). The theoretical XRD data of  $\text{Cs}_3\text{InX}_6$  were calculated using the Visualization for Electronic and Structural Analysis (VESTA) based on their crystal structures.

## Author contributions

Z. Shi and X. Chen conceived the idea for the detailed experiments. F. Zhang, X. Ji and W. Liang performed the

materials preparation experiments. F. Zhang and W. Liang carried out the TEM measurements. M. Wang, Y. Wang and Z. Ma carried out the XPS, XRD and PL measurements. F. Zhang, X. Ji and Y. Li carried out the WLED measurements. D. Wu, X. Chen and X. Li conducted the data analysis. D. Yang conducted the theoretical calculations. F. Zhang and Z. Shi co-wrote the paper. Z. Shi and C. Shan guided the whole project.

## Conflicts of interest

There are no conflicts to declare.

## Acknowledgements

This work was supported by the National Natural Science Foundation of China (No. 11774318, 12074347, 61935009 and 12004346) and the Open Fund of the State Key Laboratory of Integrated Optoelectronics (IOSKL2020KF04).

## Notes and references

- M. A. Schreuder, K. Xiao, I. N. Ivanov, S. M. Weiss and S. J. Rosenthal, *Nano Lett.*, 2010, **10**, 573.
- R. Mueller-Mach, G. O. Mueller, M. R. Krames and T. Trottier, *IEEE J. Sel. Top. Quantum Electron.*, 2002, **8**, 339.
- Z. Xia, Z. Xu, M. Chen and Q. Liu, *Dalton Trans.*, 2016, **45**, 11214.
- R. Mueller-Mach, G. Mueller, M. R. Krames, H. A. Höpfe, F. Stadler, W. Schnick, T. Juestel and P. Schmidt, *Phys. Status Solidi A*, 2005, **202**, 1721.
- Z. Shi, S. Li, Y. Li, H. Ji, X. Li, D. Wu, T. Xu, Y. Chen, Y. Tian, Y. Zhang, C. Shan and G. Du, *ACS Nano*, 2018, **12**, 1462.
- H. Cho, S. H. Jeong, M. H. Park, Y. H. Kim, C. Wolf, C. L. Lee, J. H. Heo, A. Sadhanala, N. Myoung, S. Yoo, S. H. Im, R. H. Friend and T. W. Lee, *Science*, 2015, **350**, 1222.
- C. Xie, P. You, Z. Liu, L. Li and F. Yan, *Light: Sci. Appl.*, 2017, **6**, e17023.
- M. I. Saidaminov, A. L. Abdelhady, B. Murali, E. Alarousu, V. M. Burlakov, W. Peng, I. Dursun, L. Wang, Y. He, G. Maculan, A. Goriely, T. Wu, O. F. Mohammed and O. M. Bakr, *Nat. Commun.*, 2015, **6**, 7586.
- X. Li, F. Cao, D. Yu, J. Chen, Z. Sun, Y. Shen, Y. Zhu, L. Wang, Y. Wei, Y. Wu and H. Zeng, *Small*, 2017, **13**, 1603996.
- S. Li, Z. Shi, F. Zhang, L. Wang, Z. Ma, D. Yang, Z. Yao, D. Wu, T. Xu, Y. Tian, Y. Zhang, C. Shan and X. Li, *Chem. Mater.*, 2019, **31**, 3917.
- F. Giustino and H. J. Snaith, *ACS Energy Lett.*, 2016, **1**, 1233.
- W. Pan, H. Wu, J. Luo, Z. Deng, C. Ge, C. Chen, X. Jiang, W. J. Yin, G. Niu, L. Zhu, L. Yin, Y. Zhou, Q. Xie, X. Ke, M. Sui and J. Tang, *Nat. Photonics*, 2017, **11**, 726.
- A. Wang, X. Yan, M. Zhang, S. Sun, M. Yang, W. Shen, X. Pan, P. Wang and Z. Deng, *Chem. Mater.*, 2016, **28**, 8132.
- T. C. Jellicoe, J. M. Richter, H. F. J. Glass, M. Tabachnyk, R. Brady, S. E. Dutton, A. Rao, R. H. Friend, D. Credgington, N. C. Greenham and M. L. Böhm, *J. Am. Chem. Soc.*, 2016, **138**, 2941.
- F. Locardi, M. Cirignano, D. Baranov, Z. Dang, M. Prato, F. Drago, M. Ferretti, V. Pinchetti, M. Fanciulli, S. Brovelli, L. De Trizio and L. Manna, *J. Am. Chem. Soc.*, 2018, **140**, 12989.
- B. Yang, J. Chen, S. Yang, F. Hong, L. Sun, P. Han, T. Pullerits, W. Deng and K. Han, *Angew. Chem., Int. Ed.*, 2018, **57**, 5359.
- X. Liu, X. Xu, B. Li, L. Yang, Q. Li, H. Jiang and D. Xu, *Small*, 2020, **16**, 2002547.
- B. Yang, F. Hong, J. Chen, Y. Tang, L. Yang, Y. Sang, X. Xia, J. Guo, H. He, S. Yang, W. Deng and K. Han, *Angew. Chem., Int. Ed.*, 2019, **58**, 2278.
- Y. Li, Z. Shi, W. Liang, L. Wang, S. Li, F. Zhang, Z. Ma, Y. Wang, Y. Tian, D. Wu, X. Li, Y. Zhang, C. Shan and X. Fang, *Mater. Horiz.*, 2020, **7**, 530.
- M. Leng, Y. Yang, K. Zeng, Z. Chen, Z. Tan, S. Li, J. Li, B. Xu, D. Li, M. P. Hautzinger, Y. Fu, T. Zhai, L. Xu, G. Niu, S. Jin and J. Tang, *Adv. Funct. Mater.*, 2018, **28**, 1704446.
- J. Zhang, Y. Yang, H. Deng, U. Farooq, X. Yang, J. Khan, J. Tang and H. Song, *ACS Nano*, 2017, **11**, 9294.
- L. Zhou, J. F. Liao, Z. G. Huang, J. H. Wei, X. D. Wang, W. G. Li, H. Y. Chen, D. B. Kuang and C. Y. Su, *Angew. Chem., Int. Ed.*, 2019, **58**, 5277.
- L. Zhou, J. F. Liao, Z. G. Huang, J. H. Wei, X. D. Wang, H. Y. Chen and D. B. Kuang, *Angew. Chem., Int. Ed.*, 2019, **58**, 15435.
- X. Liu, X. Xu, B. Li, Y. Liang, A. Li, H. Jiang and D. Xu, *CCS Chem.*, 2020, **2**, 216.
- P. Han, C. Luo, S. Yang, Y. Yang, W. Deng and K. Han, *Angew. Chem., Int. Ed.*, 2020, **59**, 12709.
- Y. Jing, Y. Liu, X. Jiang, M. S. Molokeev, Z. Lin and Z. Xia, *Chem. Mater.*, 2020, **32**, 5327.
- F. Zhang, D. Yang, Z. Shi, C. Qin, M. Cui, Z. Ma, L. Wang, M. Wang, X. Ji, X. Chen, D. Wu, X. Li, L. Zhang and C. Shan, *Nano Today*, 2021, **38**, 101153.
- P. Sellan, D. Liu, Y. Zhang, D. Nataraj, S. Ramya, Z. Jin, B. Mamba, A. Kuvarega and J. Gui, *ACS Appl. Nano Mater.*, 2020, **3**, 9141.
- Y. Shen, J. Yin, B. Cai, Z. Wang, Y. Dong, X. Xu and H. Zeng, *Nanoscale Horiz.*, 2020, **5**, 580.
- M. M. Yao, C. H. Jiang, J. S. Yao, K. H. Wang, C. Chen, Y. C. Yin, B. S. Zhu, T. Chen and H. B. Yao, *Inorg. Chem.*, 2019, **58**, 11807.
- G. Wu, C. Zhou, W. Ming, D. Han, S. Chen, D. Yang, T. Besara, J. Neu, T. Siegrist, M. H. Du, B. Ma and A. Dong, *ACS Energy Lett.*, 2018, **3**, 1443.
- N. F. Mott and A. M. Stoneham, *J. Phys. C-Solid State Phys.*, 1977, **10**, 3391.
- H. Peng, S. Yao, Y. Guo, R. Zhi, X. Wang, F. Ge, Y. Tian, J. Wang and B. Zou, *J. Phys. Chem. Lett.*, 2020, **11**, 4703.
- K. M. McCall, C. C. Stoumpos, S. S. Kostina, M. G. Kanatzidis and B. W. Wessels, *Chem. Mater.*, 2017, **29**, 4129.
- M. Itoh, *J. Phys. Soc. Jpn.*, 1988, **57**, 372.

- 36 A. Purdy, K. Song and A. Stoneham, *Phys. Rev. B: Solid State*, 1977, **15**, 2170.
- 37 D. Cortecchia, S. Neutzner, A. R. Srimath Kandada, E. Mosconi, D. Meggiolaro, F. De Angelis, C. Soci and A. Petrozza, *J. Am. Chem. Soc.*, 2017, **139**, 39.
- 38 C. Timmermans and G. Blasse, *Phys. Status Solidi*, 1981, **106**, 647.
- 39 Z. Ma, Z. Shi, D. Yang, F. Zhang, S. Li, L. Wang, D. Wu, Y. Zhang, G. Na, L. Zhang, X. Li, Y. Zhang and C. Shan, *ACS Energy Lett.*, 2020, **5**, 385.
- 40 Z. Z. Ma, Z. F. Shi, L. T. Wang, F. Zhang, D. Wu, D. W. Yang, X. Chen, Y. Zhang, C. X. Shan and X. J. Li, *Nanoscale*, 2020, **12**, 3637.
- 41 M. Leng, Y. Yang, Z. Chen, W. Gao, J. Zhang, G. Niu, D. Li, H. Song, J. Zhang, S. Jin and J. Tang, *Nano Lett.*, 2018, **18**, 6076.
- 42 Z. Shi, Y. Li, Y. Zhang, Y. Chen, X. Li, D. Wu, T. Xu, C. Shan and G. Du, *Nano Lett.*, 2017, **17**, 313.
- 43 Y. Toyozawa, *Prog. Theor. Phys.*, 1962, **27**, 89.
- 44 W. Stadler, D. M. Hofmann, H. C. Alt, T. Muschik, B. K. Meyer, E. Weigel, G. Müller-Vogt, M. Salk, E. Rupp and K. W. Benz, *Phys. Rev. B: Condens. Matter Mater. Phys.*, 1995, **51**, 10619.
- 45 A. Wolfert, E. W. J. L. Oomen and G. Blasse, *J. Solid State Chem.*, 1985, **59**, 280.
- 46 R. Dawson and D. Pooley, *Phys. Status Solidi B*, 1969, **35**, 95.
- 47 C. H. Leung and K. S. Song, *Solid State Commun.*, 1980, **33**, 907.
- 48 Z. Ma, Z. Shi, C. Qin, M. Cui, D. Yang, X. Wang, L. Wang, X. Ji, X. Chen, J. Sun, D. Wu, Y. Zhang, X. J. Li, L. Zhang and C. Shan, *ACS Nano*, 2020, **14**, 4475.
- 49 T. Morgan, *Phys. Rev.*, 1965, **139**, 343.
- 50 R. Zhang, X. Mao, Y. Yang, S. Yang, W. Zhao, T. Wumaier, D. Wei, W. Deng and K. Han, *Angew. Chem., Int. Ed.*, 2019, **58**, 2725.
- 51 J. Luo, X. Wang, S. Li, J. Liu, Y. Guo, G. Niu, L. Yao, Y. Fu, L. Gao, Q. Dong, C. Zhao, M. Leng, F. Ma, W. Liang, L. Wang, S. Jin, J. Han, L. Zhang, J. Etheridge, J. Wang, Y. Yan, E. H. Sargent and J. Tang, *Nature*, 2018, **563**, 541.
- 52 L. Wang, Z. Shi, Z. Ma, D. Yang, F. Zhang, X. Ji, M. Wang, X. Chen, G. Na, S. Chen, D. Wu, Y. Zhang, L. Zhang and C. Shan, *Nano Lett.*, 2020, **20**, 3568.
- 53 V. Morad, Y. Shynkarenko, S. Yakunin, A. Brumberg, R. D. Schaller and M. V. Kovalenko, *J. Am. Chem. Soc.*, 2019, **141**, 9764.
- 54 M. Li, J. Zhou, G. Zhou, M. Molokeev, J. Zhao, V. Morad, M. Kovalenko and Z. Xia, *Angew. Chem., Int. Ed.*, 2019, **58**, 18670.
- 55 Y. H. Kim, H. Cho and T. W. Lee, *Proc. Natl. Acad. Sci. U. S. A.*, 2016, **113**, 11694.
- 56 S. D. Stranks, V. M. Burlakov, T. Leijtens, J. M. Ball, A. Goriely and H. J. Snaith, *Phys. Rev. Appl.*, 2014, **2**, 34007.
- 57 M. D. Smith and H. I. Karunadasa, *Acc. Chem. Res.*, 2018, **51**, 619.
- 58 J. P. Perdew and M. Levy, *Phys. Rev. Lett.*, 1983, **51**, 1884.
- 59 M. G. Ju, J. Dai, L. Ma, Y. Zhou and X. C. Zeng, *J. Am. Chem. Soc.*, 2018, **140**, 10456.
- 60 H. Yang, T. Cai, E. Liu, K. Hills-Kimball, J. Gao and O. Chen, *Nano Res.*, 2020, **13**, 282.
- 61 J. L. Xie, Z. Q. Huang, B. Wang, W. J. Chen, W. X. Lu, X. Liu and J. L. Song, *Nanoscale*, 2019, **11**, 6719.
- 62 R. Zhang, X. Mao, D. Zheng, Y. Yang, S. Yang and K. Han, *Laser Photonics Rev.*, 2020, **14**, 2000027.
- 63 C. Zhou, Y. Tian, M. Wang, A. Rose, T. Besara, N. K. Doyle, Z. Yuan, J. C. Wang, R. Clark, Y. Hu, T. Siegrist, S. Lin and B. Ma, *Angew. Chem., Int. Ed.*, 2017, **56**, 9018.
- 64 Z. Ma, L. Wang, X. Ji, X. Chen and Z. Shi, *J. Phys. Chem. Lett.*, 2020, **11**, 5517.
- 65 M. Shimizu, M. Koshimizu, Y. Fujimoto, T. Yanagida, S. Ono and K. Asai, *Opt. Mater.*, 2016, **61**, 115.
- 66 D. B. Straus, S. Hurtado Parra, N. Iotov, J. Gebhardt, A. M. Rappe, J. E. Subotnik, J. M. Kikkawa and C. R. Kagan, *J. Am. Chem. Soc.*, 2016, **138**, 13798.
- 67 J. Luo, M. Hu, G. Niu and J. Tang, *ACS Appl. Mater. Interfaces*, 2019, **11**, 31575.